Processes contributing to Arctic cloud dissipation and formation events that bookend clear sky periods

Joseph Sedlar[1,2], Adele Igel[3], Hagen Telg[1,2]

[1]Cooperative Institute for Research in Environmental Sciences, University of Colorado Boulder, Boulder, CO, USA
5 [2]NOAA Global Monitoring Laboratory, Boulder, CO, USA
[3]University of California Davis,

Correspondence to: Joseph Sedlar (joseph.sedlar@colorado.edu)

Abstract. The Arctic is predominantly cloudy with intermittent clear sky periods. These clear periods have profound impacts on the surface energy budget and lower atmospheric stratification, connected to a lack of downwelling longwave radiation in 10 the absence of cloud. Despite the importance of clear sky conditions, an understanding of the atmospheric processes leading to low-level cloud dissipation and formation events is relatively limited. A strict definition to identify clear periods at Utqiagvik (formerly Barrow), Alaska, during a five-year period (2014-2018) is developed. A suite of remote sensing and in situ instrumentation from the high-latitude observatory are analysed; we focus on comparing and contrasting atmospheric properties during low-level cloud dissipation and formation events to understand the processes controlling clear sky periods. 15 Vertical profiles of lidar backscatter suggest that aerosol presence across the lower atmosphere is relatively invariant around the clear period bookends, which suggests that a sparsity of aerosol is not frequently a cause for cloud dissipation. Further meteorological analysis indicates two active processes ongoing that appear to support the formation of low clouds after a clear sky period and have a link to surface aerosol concentrations; namely, horizontal advection which was dominant in winter and early spring and quiescent air mass modification which was dominant in the summer. During summer, the 20 dominant mode of cloud formation is a low cloud/fog layer developing near the surface. This low cloud formation is driven largely by air mass modification and pooling of aerosol particles near the surface under lower-atmosphere stratification.

1 Introduction

Over the Arctic clouds are ubiquitous (e.g., Herman and Goody, 1976). Studies of cloud occurrence from satellite report 25 large cloud fractions over the full annual cycle (Wang and Key, 2005; Kay et al., 2016). Detailed observations of the vertical structure of Arctic clouds from remote sensing "supersites" document the frequent presence of lower tropospheric clouds (e.g., Shupe et al., 2011). These clouds frequently contain concentrations of both liquid- and ice-phase particles, known as mixed-phase clouds, which can persist for hours to even days in a near homogeneous state (Shupe, 2011). Liquid-bearing clouds are observed during all seasons at temperatures as cold as -34 °C (Intrieri et al., 2002) but liquid is most common 30 during the summer months (Shupe et al., 2011). Clouds strongly modulate the incoming and outgoing radiative fluxes; over

sea ice, longwave radiation dominates the radiative energy budget at the surface (Walsh and Chapman, 1998; Shupe and Intrieri, 2004; Sedlar et al., 2011).

35 While clear sky periods are less frequent than cloudy periods in the Arctic, their impact on surface radiation and thermodynamic structure are also considerable. So-called radiative states are dominant features of the Arctic atmosphere, alternating between radiatively clear and radiatively opaque states (Stramler et al., 2011). The Arctic atmosphere is relatively dry and cold, limiting the atmospheric greenhouse effect when clouds are absent. The surface longwave warming associated with Arctic clouds, or lack thereof, is a crucial component of the surface energy budget in the Arctic (Walsh and Chapman, 1998; Shupe and Intrieri, 2004; Sedlar et al., 2011). Under cloud free conditions, effective infrared cooling from the surface

40 causes extremely cold near-surface temperatures (Pinto et al., 1997). As a result, strong surface-based temperature inversions commonly form (Kahl, 1990), and the turbulent mixing in the surface layer is inhibited. The Arctic boundary layer tends to remain relatively shallow following the lack of buoyant mixing, which is currently understood to be caused primarily by the turbulent energy production associated with radiative divergence near the top of mixed phase stratocumulus (Shupe et al., 2008; Shupe et al., 2013; Sedlar and Shupe, 2014; Sotiropoulou et al., 2014; Brooks et al., 2017; Tjernström et al., 2019).

45 Over sea ice, when skies are clear, the surface energy deficit can lead to anomalies in the ice growth or ice melt depending upon season (Sedlar and Devasthale, 2012). Global climate models that fail to properly represent the seasonal occurrence of Arctic low-level stratocumulus also fail to match the observed relationships amongst net surface radiative forcing and static stability (Pithan et al., 2014).

50 Morrison et al. (2012) report that the transition between the radiative states is controlled by the evolution of lower tropospheric clouds in the Arctic. As such, there is great interest in understanding the processes and mechanisms crucial to the formation, maintenance, and dissipation of lower tropospheric Arctic clouds. Their persistence seems counterintuitive since mixed-phase clouds are microphysically unstable (Morrison et al. 2012). Few studies have examined the processes active during dissipation and formation of these clouds. Simulations of Arctic clouds consistently show that over-abundant

55 ice nuclei or ice crystal concentrations can lead to cloud glaciation (Harrington et al. 1999; Jiang et al. 2000; Avramov and Harrington, 2010; Morrison et al. 2011). Simulations also suggest that very low cloud condensation nuclei (CCN) or cloud droplet number concentrations (~ 10 cm^{-3} or less) may result in cloud dissipation (Birch et al., 2012; Loewe et al., 2017; Stevens et al., 2018). Based on observations from the North Slope of Alaska (NSA) and complementary simulations, Silber et al. (2020) hypothesize that low aerosol concentrations may also slow or inhibit the formation of turbulent liquid-bearing

60 clouds from their optically thin, nonturbulent predecessors.

A detailed analysis of an Arctic cloud dissipation event suggested a myriad of complex processes contributed to the cloud decay (Kalesse et al., 2016). Observed changes in aerosol number and scattering properties were found to be associated with a large-scale change in air mass that advected through the NSA region. Their case study revealed how transient atmospheric

65   dynamics were responsible for changing the thermodynamic structure, coinciding with a response in the cloud microphysical properties. They suggest that the interaction of aerosol-modified cloud microphysical properties with dynamic and thermodynamic processes could be important for driving dissipation. The results of Kalesse et al. (2016) are far from the steady state, idealized modelling studies that typically focus on how changes in aerosol or cloud particle concentrations impact cloud lifecycle.

70

In that regard, it is important to better understand the causes that lead to the cloud dissipation and subsequent cloud formation events which bookend the clear sky periods. In this paper, we examine the characteristics of clear-cloudy sky transitions in the Arctic. More specifically, we assess whether the aerosol and the general meteorological variability provide clues to the processes that are important for low cloud dissipation and cloud formation events. By comparing and contrasting

75   the variability of such properties shortly after cloud dissipation (start of clear period) and shortly prior to cloud formation (end of clear period), we aim to learn how changes in aerosol number, aerosol vertical partitioning, and atmospheric thermodynamics contribute to formation and cessation of clear sky periods in the Arctic. Measurements and retrievals from a range of in situ and remote sensing instruments during the course of a five-year period from 2014-2018 on the NSA at Utqiagvik (formerly Barrow) are utilized. Rather than exploit individual cases, we assess the role of aerosol, synoptic

80   variability and near-surface meteorology using a statistical approach for strictly defined clear sky periods over these five years.

2 Instruments

The Vaisala CL31 ceilometer is an operationally robust instrument measuring the vertical profile of backscattered light due

85   to aerosol and cloud particles (Ravila and Räsänen, 2004). The lidar instrument operates fully automatically by emitting a pulsed laser with a wavelength of 910 nm. The backscattered signal is processed by onboard software, producing retrievals of cloud presence and the vertical level of up to 3 cloud base heights. When the signal is attenuated but a cloud base height could not be retrieved, the retrieval software assumes the obscuration in the backscatter is due to a surface-based cloud or fog layer and therefore reports the vertical visibility.

90

The high spectral resolution lidar (HRSL, Eloranta, 2005) was designed to separate the molecular scattering signal from the geophysical (aerosol, cloud) scattering signals at the 532 nm laser wavelength. As a result, vertical profiles of aerosol and cloud hydrometeor backscatter are robustly characterized by the instrument retrieval software. Profiles of particulate (aerosol + cloud) backscatter and depolarization ratio are used to aid in identification of clear sky profiles, in addition to examining

95   the vertical distribution of aerosol during clear sky periods. Because the HSRL operates in the visible light portion of the spectrum, the signal becomes attenuated once the cloud optical thickness reaches ~ 3 to 4.

Vertical distributions of cloud layers were derived from the zenith-viewing Ka-Band (KAZR) cloud radar (e.g., Moran et al., 1998). The KAZR measures the spectra of backscattered power (reflectivity) as a function of Doppler velocity of the cloud and precipitation particles in the atmospheric column above the radar. The millimeter wavelength (35 GHz) provides high sensitivity and signal to noise ratio allowing the radar to observe small concentrations of small cloud droplets. The ARSCL (Active Remote Sensing of Cloud Layers) processing algorithm (Kollias et al., 2016) produces processed KAZR cloud property retrievals based on best-estimate radar moments including reflectivity, Doppler velocity, and spectrum width. Cloud top height and signal to noise ratios from the ARSCL data products are examined here.

At the surface, a TSI 3010 condensation particle counter measures the number of particles present within a volume of air with diameters of 10 to 3000 nm. Air is continuously pumped through the instrument, where an alcohol solution is added to produce condensational growth on the individual particles. If the particles grow to a diameter above 0.01 um, they scatter light emitted by a laser diode and can then be counted by an optical particle detector.

Near-surface measurements of air temperature, dew point temperature, and wind speed and direction were observed from a weather station deployed on the NSA. Downwelling and upwelling longwave radiation measurements were made from upward- and downward-viewing Eppley Precision Infrared Pyrgeometers. These instruments have factory stated uncertainties of about 4 W m^{-2}. The longwave fluxes are further scrutinized using the Radiative Flux (e.g., Long and Turner, 2008) processing retrievals.

Atmospheric profiles of thermodynamics and winds were made by radiosoundings launched from the NSA. Radiosoundings were launched nominally every 12 hours, although intermittent periods exist when the frequency was either higher or lower. The measurements of temperature, specific humidity, and pressure were used to compute profiles of equivalent potential temperature.

3 Methods

Measurements from the instrumentation described above are analysed to characterize and better understand radiative, aerosol, and thermodynamic characteristics of clear sky periods on the NSA during all seasons from 2014 through 2018. The identification of clear sky periods is first and foremost dependent upon continuous measurements from the ceilometer. Periods of continuous ceilometer detection status equal to zero (zenith-viewing clear sky) were earmarked as potentially clear. To avoid broken cloudiness being classified as clear periods, clear sky periods were required to be at least 2 hours in duration. If the 2-hr temporal requirement was met, the end of the clear period was determined as the point where a cloudy

detection status (greater than zero) re-emerged and persisted for at least 2 consecutive hours. The start and end times of the
130 clear periods meeting these criteria were logged. Clear periods were scrutinized further by ensuring at least 96% of the
ceilometer detection status during the clear period were actually reported as clear sky. If intermittent cloudiness occurred and
this condition was not met, the clear period was discarded from further analysis. Based on this definition, our analysis is
focused on strictly defined clear sky periods. Finally, clear periods are required to be bookended by clouds below 2 or 3 km
(depending on the analysis below) or less in order to focus on the dissipation and formation of low-level clouds.

135

Start and end times of the clear periods were compiled monthly for further cloud screening. Measurements from the HSRL
and cloud radar during identified clear periods were exploited to further modify start and end times of clear periods based on
their sensitivities to cloud hydrometeors. Vertical profiles of HSRL backscatter and depolarization ratio during each clear
period were scrutinized to modify start and end times when backscatter and depolarization ratio exceeded threshold values
140 typical of aerosol particles in the Arctic (Shupe, 2007). Signal to noise ratios and minimum detectable reflectivity flag
indicators from the cloud radar were used to further remove times of intermittent cloud and/or precipitation signals during
the clear periods. An identified clear period having a start or end time that transitioned between adjacent months was
considered for analysis in both months.

145 An example clear sky period from 14 August 2014 is shown in Fig. 1. Prior to the start of the clear sky period, a low cloud
with base and top heights between 100 and 400 m AGL was present. The clear period began shortly before 04:00UTC and
persisted for nearly 9 hours before intermittent, very low cloud signatures were observed by the cloud radar, HSRL, and
ceilometer (Fig. 1a-b). The transition from cloudy to clear caused marked transitions in the net surface radiative fluxes,
especially in the net longwave (LWN) which dropped by nearly 80 W m^{-2} (Fig. 1c); a similar abrupt transition in LWN
150 occurred together with the low cloud formation shortly before 13:00UTC. The abrupt changes in LWN in Fig. 1c are
representative examples of the radiative states governing the Arctic (Stramler et al., 2011; Morrison et al., 2012; Engström et
al., 2014). The inset of Fig. 1c shows the equivalent potential temperature profiles from radiosoundings during the event at
05:30 (blue) and 13:15UTC (yellow), revealing changes in mixed layer depth depending upon whether or not the cloud was
present; decreases in mixed layer depth are evident in the shallower layer depth of aerosol backscatter from the HSRL during
155 the clear period (Fig. 1b). Evolution of near-surface meteorology showed modest changes in the thermodynamics and
predominant wind direction, especially around the times of cloud dissipation and formation (Fig. 1d). Likewise, near-surface
particle concentrations exhibited the largest variability near the start and end of the clear period (Fig. 1e).

The following sections explore the statistical variability of aerosol and meteorology associated with clear sky periods on the
160 NSA from 2014 through 2018.

4 Results

4.1 Clear sky periods

The number of periods meeting the strict, clear-sky criteria are relatively few over the 2014-2018 period, owing to the vast
165   persistence of Arctic cloudiness. Clear periods were most frequent during the dark winter and spring months, reaching a
maximum of over 24 individual periods during spring; increased cloudiness during the summer and autumn seasons limited
clear sky periods to as few as six (Fig. 2) based on the strict definition of a clear sky period here. The annual distribution of
monthly clear sky frequency follows the annual trends of cloudiness in the high Arctic reported in the literature (Curry et al.,
1996; Wang and Key, 2005; Shupe, 2011), where more clear periods are found during the seasons with relatively lower
170   cloud fractions.

Figure 2 also highlights the number of these clear periods that end by the emergence of a low cloud layer (magenta bars),
defined as ceilometer-retrieved cloud base below 400 m AGL, or the ceilometer operating in vertical visibility mode which
identifies a surface-based fog layer. There is a clear seasonal cycle in the emergence of low clouds or fog, which dominate
175   the clouds that emerge after clear periods from spring through early autumn. We will focus on these low cloud forming cases
in subsequent sections in order to understand the processes supporting the formation of low clouds after a clear sky period.

4.2 Aerosol characteristics at clear period bookends
4.2.1 HSRL aerosol backscatter during clear periods

180   Lower tropospheric Arctic clouds require the availability of aerosol that act as cloud condensation nuclei and ice nuclei.
Here, the statistical distributions of aerosol backscatter during clear periods from the HSRL are examined to determine if the
vertical structure of aerosol may provide clues to processes supporting dissipation or formation of clouds that bookend the
clear periods.

185   The vertical structure of aerosol backscatter retrieved from the HSRL during all clear periods as a function of month is
presented in a climatological fashion. From Fig. 3, it is found that aerosol backscatter has a very dynamic structure, with
variability changing both vertically and temporally (Kafle and Coulter, 2013). Largest aerosol backscatter occurs near the
surface and decreases with height until a level of maximum variability (the 1-σ envelope) is encountered, often within the
atmospheric layer between a few hundred meters and 1 km. Above this level of peak variability, backscatter makes a
190   transition towards a quasi-constant magnitude with height representative of the free troposphere. The gradient transition level
is highest from winter and mid-spring (a-d), while it is shallowest during later spring and through summer (e-j). Many
processes may contribute to the depth of the enhanced aerosol backscatter layer, including horizontal advection, long-range

transport often largest during winter (Klonecki et al., 2003; Willis et al., 2018), and lower atmosphere stratification; likely the large variability across the lowest kilometer is related to a combination of these characteristics.

195

Figure 4 is similar to Fig. 3 but only includes backscatter profiles within an hour after cloud dissipation and an hour before formation across the lowest 1400 m for four selected months, representative for each season. Median and interquartile ranges are shown only for cases when the cloud formation at the end of the clear period was a low cloud or fog, which limits the number of profiles included in the statistics (see Fig. 2, magenta bars). Only modest differences in aerosol backscatter just

200 after cloud dissipation (black, gray) and just before cloud formation (blue, light blue) are noted and overall the profiles are very similar to those for the full clear sky periods (Fig. 3); most obvious is a reduction in backscatter in November just before cloud formation (Fig. 4d).

It is interesting that the level where backscatter transitions to its quasi-constant value is at or above where low cloud

205 formation (base < 400 m or surface fog) occurred. For April and July (Fig. 4b-c) this is true even for the backscatter profile just after the beginning of the clear period (black/gray envelope). Consistency in aerosol backscatter structure from start to end of these clear periods seems to mimic the behaviour of a residual layer of relatively well-mixed aerosol trapped across the lowest few hundred meters of the atmosphere. This mixed layer may have been an artifact of the previous sub-cloud mixed layer prior to dissipation. Studies have shown such a mixed layer is present in connection with turbulence driven by

210 cloud-generated buoyant overturning associated with lower atmosphere Arctic clouds containing supercooled liquid (Morrison et al., 2012; Shupe et al., 2013; Sedlar and Shupe, 2014; Sotiropoulou et al., 2014). We note that the lowest effective range height of the HSRL is approximately 105 m AGL and therefore impossible to infer whether consistent changes in aerosol are ongoing closer to the surface. Nonetheless, since the transition to a quasi-constant value is occurring at or above cloud base, the data suggest that surface aerosol properties such as number concentration are likely often

215 unrepresentative of aerosol properties at cloud level (e.g., Creamean et al., 2020).

The similarity of backscatter profiles just after cloud dissipation to those just before formation, and to the entire period, suggests the cloud-free periods are not regularly caused by a void of aerosol presence as has been hypothesized to be possible at least occasionally in the high Arctic (Birch et al., 2012; Loewe et al., 2017; Stevens et al., 2018). To better

220 connect vertical partitioning of aerosol backscatter to potential impacts on cloud dissipation and formation, backscatter profiles are normalized by mean cloud top height retrieved from the ARSCL processing of cloud radar profiling. Only cases where a mean cloud top below 2 km AGL before cloud dissipation and after cloud formation are examined; the cloud top height is used to normalize backscatter profiles in a window 1-hr after/before a cloud dissipation/formation event. Statistical distribution profiles of backscatter on a common vertical grid for February through May are presented (Fig. 5) because these

225 months had the most frequent clear sky periods (more robust statistics), but also these months mark a seasonal transition to predominantly low cloud formation after the clear periods (see Fig. 2). Because the lidar is attenuated by cloud, it is

impossible to examine aerosol backscatter characteristics prior to cloud dissipation or after cloud formation. This is true both above the cloud layer, as well as in the sub-cloud layer because low-level Arctic clouds frequently precipitate ice crystals and drizzle droplets (Shupe et al., 2004; Shupe, 2011) and these hydrometeors dominate the backscatter compared to that
230 from aerosol.

In the hour after cloud dissipation, aerosol backscatter decreases with height with relative maxima and minima backscatter occurring near the surface and near the prior cloud top level, respectively, and above (Fig. 5a-d); the decreasing backscatter profile is less evident during May, a feature that remains through the subsequent summer and early autumn months (not
235 shown). These profile shapes are similar to the decrease with height found for the full clear period profiles of backscatter for the winter and spring months (Fig. 3). Values of backscatter larger than 10^{-7} m^{-1} sr^{-1}, a value used as a cutoff between aerosol and clear sky (Shupe, 2007) at all heights suggests that aerosol concentrations remained relatively large within or below the previous cloud level. Thus, aerosol particles were present within the sub-cloud layer even after the cloud dissipated (or perhaps because the cloud dissipated), again suggesting that a lack of particles from below the cloud was not regularly the
240 likely cause for dissipation.

Being that aerosol backscatter near and above cloud top (z_n=1) was at a minimum suggests that low aerosol concentrations near cloud top could have played a role in its dissipation. Model simulations have found that free tropospheric aerosol can be entrained into the cloud layer and may be an important source for CCN/IN (Igel et al., 2017). However, low aerosol
245 concentrations at cloud top are unlikely to contribute to cloud dissipation unless concentrations below cloud base are also very low. This seems unlikely to be the case based on Fig. 5. Furthermore, in the hour before clouds form at the cessation of a clear period, aerosol backscatter distributions are substantially flatter (Fig. 5e-f), revealing less of a decreasing tendency with height. The dominant mode of the backscatter RFDs typically agrees in magnitude with the minimum values at and above z_n=1 just after cloud dissipation (Fig. 5a-d). These characteristics in the backscatter profiles indicate that aerosol
250 concentrations aloft are likely high enough to support clouds, and thus low concentrations are not frequently preventing the formation of new cloud layers.

4.2.2 Near-surface aerosol concentrations and clear period boundaries

Variability in near-surface particle concentrations around the bookends of clear periods are investigated to complement the
255 lidar analysis. Monthly median and interquartile ranges within 2-hr after cloud dissipation versus before cloud dissipation reveal distinct seasonal and temporal dependencies (Fig. 6a-d). In terms of number concentrations, lower quartile values are frequently 10 cm^{-3} or less. More particles are found in summer and early autumn than during winter and spring. However, seasonal differences in particles from surface measurements are different from the vertical backscatter across the lowest 1 km, where winter and spring backscatter were statistically larger than summer and early autumn (Fig. 3), again suggesting a
260 disconnect between what is measured at the surface versus measured aloft. Additionally, there is very little change in the

median or 25th-75th percentile range of particle concentrations leading up to cloud dissipation compared to after dissipation during winter and spring (Fig. 6a-b). Oppositely, concentrations were almost always larger after clouds had dissipated during summer and early autumn (Fig. 6c-d). Having the same or greater number concentration after the clear period starts is the reverse of what is expected if decreasing aerosol concentrations are driving cloud dissipation.

265

Similarly, CPC concentrations leading up to, and shortly after, cloud formation (end of clear period) are shown in Fig. 6e-h. Only cases when the forming cloud layer was identified as a low cloud or surface fog with cloud base below 400 m are considered here; this distinction was made in an effort to constrain the vertical footprint of the near-surface CPC measurements. While very small differences in concentrations surrounding the cloud formation events during winter are

270 observed, a tendency for decreased particle concentrations after cloud formation in summer and autumn is observed, as well as for some spring events. These results suggest a connection between an abundant presence of aerosol particles and potentially these particles serving as the sources of CCN activation in the lower atmosphere. The fact that particle concentrations drop after cloud formation, in some cases by over a factor of two (see summer medians in Fig. 6g), supports the mechanism of a conversion of a fraction of these particles to low cloud/fog droplets.

275 **4.3 Meteorology and its relationship to clear periods**

The previous analyses failed to identify drastic signal changes in the vertical distribution or surface concentration of aerosols surrounding cloud dissipation and formation events. Therefore, the results imply that cloud-free periods may not be driven by significant changes in aerosol presence alone, consistent with conclusions drawn from an Arctic dissipation case examined in detail (Kalesse et al., 2016). Here we investigate meteorological phenomena to understand their role in

280 supporting cloud-free events via their contribution to cloud dissipation and/or formation processes as well as their role in modulating surface aerosol concentrations. In this section, emphasis is given to understanding the processes supporting low cloud formation (base below 400 m) as these are the dominant cloud type emergent after clear sky periods during much of the year (Fig. 2).

285 **4.3.1 Clear skies, cloudy skies and lower tropospheric stability**

Arctic stratocumulus clouds exert a critical influence on the static stability near the surface, where these clouds often modulate the stratification due to sub-cloud mixing driven by cloud-top turbulence (Shupe et al., 2008, 2013; Sedlar, 2014; Sedlar and Shupe, 2014; Brooks et al., 2017). A metric to explore the influence of clouds on stratification is through the relationship between lower tropospheric stability (LTS) and net longwave (LWN) radiation. This parametric relationship has

290 the potential to identify coupled modes in the data since LWN is primarily proportional to cloud liquid (cloud infrared emissivity) and surface temperature, while the difference in equivalent potential temperature between the surface and 950 hPa pressure level provides a value on the static stability of the lower troposphere (Sedlar et al., 2020). The 950 hPa level is

generally around 500 m AGL in the Arctic, which frequently encompasses all, or a fraction of, the Arctic atmospheric boundary layer and the sub-cloud mixed layer (Shupe et al., 2013; Sedlar and Shupe, 2014).

295

The strong dependence of LWN on the presence or absence of clouds (see Fig. 1c), and the strong linkage between cloud and stratification (LTS) is evident in the seasonal RFDs in Fig. 7a-d). The dominant peak in the seasonal distributions occurs for LWN near -10 Wm^{-2} and LTS ranging from 0 to 2.5 K, corresponding to near-neutral to slightly stable stratification; this mode represents the canonical overcast Arctic with cloud-generated turbulence producing mixing across the boundary layer

300   and sub-cloud mixing layer (Sedlar et al., 2020).

The red symbols correspond to instances in the LWN-LTS parameter space when a radiosounding was launched during a clear period. These symbols correspond to a far less frequently occurring distribution mode occurring under clear skies, with larger (< -40 Wm^{-2}) LWN deficits and correspondingly greater positive LTS. The surface is cooling effectively to space, and

305   together with the lack of mixing from the absence of low-level liquid-bearing clouds, an enhanced stable stratification is maintained across the lower troposphere. Differences in the magnitudes of both the clear-sky LWN and LTS modes by season are connected to thermodynamic constraints dependent upon annual cycle. For example, LWN deficits are considerably larger in summer than winter and spring because the land surface at Barrow emits infrared radiation at a much warmer temperature. Positive LTS for clear-sky conditions are smaller in magnitude during summer than winter and spring

310   because shortwave radiation represents a strong surface energy forcing, dependent upon surface albedo and solar elevation.

RFDs describing the relationship between surface condensation particle counts (CPC) per LTS are shown in Fig. 7e-h. CPC distributions for winter and spring (e-f) are invariant to the stratification, indicating that near-surface aerosol numbers are largely independent of sky condition (clear or cloudy). The spread in CPC concentrations increases during summer and

315   autumn, where an order of magnitude span in the distributions are observed (g-h). During summer and autumn, it is evident that CPC concentrations were consistently larger during clear sky periods (red symbols) than during cloudy conditions (concentrations corresponding to the peak mode in the RFD with LTS < 2.5 K). These seasonal and sky condition differences in particle concentrations suggest different mechanisms are responsible for aerosol numbers near the surface.

320   **4.3.2 Meteorological contributions to cloud formation**

Tendencies in near-surface air temperature and dew point depression (dew point temperature minus air temperature) leading up to low cloud/fog formation events are calculated and presented in Fig. 8. These signals in near-surface thermodynamics may provide insight into the processes supporting low cloud/fog layer formation at the completion of clear sky periods. Beginning with air temperature, a decreasing trend is found for the majority of cases, regardless of month. During these clear

325   periods, the atmosphere is strongly transparent to longwave radiation emitted from the surface, and the lack of clouds to re-emit longwave back to the surface results in persistent temperature drops. From the 4-hr period prior to cloud formation

(final 4-hr of a clear period), air temperatures changed primarily at a rate between 0 and 1°C hr^{-1}. The scatter plots reveal that positive temperature trends also occurred for a handful of cases. Other ongoing processes besides quiescent surface longwave cooling, such as heat advection or solar heating, likely contributed to the positive temperature trends during the

330   final hours of these respective clear periods.

Dew point depressions are then computed; a positive tendency (linear trend) signifies a reduction in the difference between air temperature and dew point temperature, and opposite for a negative tendency. In winter and autumn (Fig. 8a, d), dew point depression trends hover primarily around 0°C hr^{-1}, with some outliers as exceptions. Therefore, regardless of the trend

335   in air temperature, the dew point temperature change during these periods often follows the same magnitude and sign; as such, when air temperature decreases the moisture content must also decrease, and vice versa with increasing temperature. This signal is representative of thermodynamic changes resulting from air mass changes through advection.

The behaviour persisted into early to mid-spring where relatively small dew point depression trends continued despite the

340   emergent dominance of negative air temperature trends (Fig. 8b). This pattern shifted in May and through the rest of summer. Here, the scatter plots indicate the trends in air temperature and dew point depression generally lie around the dashed 1:1 line, especially during summer (Fig. 8c). Cases with a positive dew point depression trend and negative air temperature trend represent an increase in relative humidity in the near-surface measurements. This emergent summertime signal indicates an increased near-surface moisture burden ongoing across the final 4 hours of the clear period.

345

The variability in near-surface wind direction and wind speed at the start and end of the clear periods as a function of season is shown in Fig. 9. Analysis is restricted to only clear periods that were followed by the formation of a low cloud or fog layer (same cases as in Fig. 8). From spring through autumn (b-d), wind direction RFDs within a 1 hr period just after dissipation (blue) and 1 hr just prior to cloud formation (red) indicate little change in the air mass origination near the surface. A

350   dominant east-northeast wind prevailed through summer during these clear periods, while autumn winds were influenced by an enhanced southerly component. Spring and summer near-surface winds predominantly have an ocean footprint, which is likely influenced by sea ice cover during spring and more open water during summer. Wind direction variability was considerably larger during winter between the beginning and end of the clear periods (Fig. 9a); large wind shifts in winter are representative of synoptic scale variability and frontal passages.

355

A lack of wind direction variability in spring and summer indicates more persistent flow patterns for the duration of the clear periods. This suggests that large-scale synoptic forcing is not often the driver for cloud dissipation and subsequent cloud formation. Wind speed distributions (inserts in Fig. 9) were relatively consistent between the start and end of clear periods in terms of the peak wind speeds. Relatively constant wind direction and wind speed at the start and end of the clear periods

360   further support the finding of persistent flow during spring and summer. Wind speed distribution width was slightly larger

prior to cloud formation (blue) compared to dissipation (red) during winter (insert in Fig. 9a), while during spring and summer the width of the distribution was larger after dissipation (insert in Fig. 9b-c).

Despite relative consistency in near-surface winds during clear periods, larger-scale atmospheric dynamics are likely

365   governing the processes leading to cloud dissipation and formation (Kalesse et al., 2016). To determine the presence and strength of large-scale advective forcing, tendencies in geopotential thickness between two atmospheric pressure layers before cloud dissipation and before cloud formation are analysed. Geopotential thickness between pressure levels is proportional to the mean temperature and mean moisture content of the layer, and therefore are indicators of change in layer temperature, moisture, or both.

370

Theoretically, geopotential tendency is related to both vorticity advection and geopotential advection (resulting from thermal advection) through quasi-geostrophy (e.g., Holton, 1992). In practice, we can estimate the general structure of geopotential by computing the geopotential thickness from radiosounding profiles at Barrow for two atmospheric layers: 1) the 500-700 hPa layer, and 2) the adjacent 700-850 hPa layer. Comparing the tendencies in these two layers are then useful for

375   identifying differential thermodynamic advection which can be linked to the instability and the vertical coherency of dynamic forcing. To compute height tendencies, we take the two radiosounding profiles nearest to in time, but not after, the cloud dissipation time and compute the change in geopotential height per time between profiles (m hr^{-1}). In a similar fashion, the geopotential height tendencies are computed for the two profiles prior to, but not after, the cloud formation time (end of clear period). Here we require that at least one of these radiosoundings was launched within the clear period (this reduced the

380   number of cases because soundings were nominally launched every 12 hours).

Scatter plots of geopotential height tendencies in the 500-700 hPa layer against the 700-850 hPa layer are shown in Fig. 10. First, geopotential height tendencies are in flux; instances when the height tendencies in both layers were small are the minority. Solely from a magnitude standpoint, these tendencies suggest the layer thermodynamics are constantly impacted

385   by transient atmospheric disturbances.

Plotting the layer tendencies as a scatter plot reveals when mean thermodynamic changes in the layers was homogeneous (same sign), or driven by barotropic-like disturbances, or whether thermal advection across these layers was differential (opposite sign), or driven by baroclinic-like disturbances. We find that, prior to cloud dissipation, geopotential height

390   tendencies between the two atmospheric layers frequently followed the same sign from November (Fig. 10d) through April (Fig. 10a-b); least squares linear regression of the tendencies between the layers reveal a moderate agreement to the monthly cases, with correlations in the 0.44 to 0.72 range. Cloud dissipation events during these months are therefore frequently impacted by relatively homogeneous thermal advection across the lower to mid-troposphere.

395 From May (Fig. 10b) through summer (Fig. 10c), differential advection amongst the atmospheric layers becomes a more frequent occurrence. Differential advection causes height tendency increases (decreases) in one layer, while the adjacent layer experiences height decreases (increases). This pattern is representative of developing or decaying baroclinic disturbances and suggests evolving synoptic forcing is potentially governing cloud dissipation during the summer.

400 Qualitatively, the results are similar for the geopotential height tendencies leading up to cloud formation (Fig. 10e-h); the atmospheric layers are prone to height variability likely resulting from synoptic activity. Homogeneous, barotropic-like height tendencies between 500-700 hPa and 700-850 hPa were most frequent and most robust (r = 0.7 - 0.8) in winter (Fig. 10e). Additionally, prior to wintertime cloud formation events, height tendencies across the 700-850 hPa layer were generally contained within the $\pm$ 1 m hr^{-1} (an exception being February), which is smaller than the range observed prior to

405 cloud dissipation (Fig. 10a). Analogously, a reduction in the range in height tendencies during spring in the 500-700 hPa layer occurred for pre-dissipation (b) and pre-formation (f) events, while similar ranges remained across the lower layer. The summer months were still influenced by active differential advection (Fig. 10g). While the tendencies in the upper layer remained approximately as large in pre-formation (g) cases as in pre-dissipation (c) cases, the lower layer tendency range is reduced.

410

In Fig. 10e-h, tendencies preceding the formation of a low cloud/fog layer are plotted as squares to differentiate from higher level cloud formations. During winter and spring, more squares are found with smaller absolute height tendencies compared to the circles. Therefore, we identify that the height level where cloud formation events occur may be influenced by a weaker synoptic setting from December through May. However, in summer nearly all clear periods are followed by the formation of

415 low clouds and/or fog, and therefore we cannot distinguish these events in terms of synoptic variability.

5 Discussion

The statistical analyses presented fail to identify a definitive signal in aerosol vertical profiles indicating changes in aerosol partitioning are the primary cause for cloud dissipation. Aerosol backscatter was lower near the former cloud level compared

420 to below, possibly hinting that a change in air mass, and associated aerosol properties, may have contributed to dissipation. However, climatologies from HSRL profiles indicate aerosol particulate backscatter is always higher nearer the surface than near cloud level. This is consistent with the surface being the primary source for airborne aerosols and highlights the need for more vertical information about aerosol particles. The complicated nature of boundary layer mixing processes in the Arctic due to a lack of ground-based convection and general stable stratification further enforce this gradient structure in

425 HSRL backscatter (Di Pierro et al., 2013; Kafle and Coulter, 2013).

Larger-scale differential advection is almost always ongoing prior to cloud dissipation, and as such it is assumed that different air mass origin and thermodynamic properties are likely to go in unison with changing aerosol properties. Median values of clear sky HSRL backscatter were similar amongst all seasons, although the variability in HSRL aerosol backscatter

430   profiles over the lowest kilometer was larger in winter and spring than in summer. Horizontal advection was found to be stronger during the former seasons, suggesting that transient dynamics likely contribute to the observed variability of aerosol vertical partitioning through transport processes.

Near the surface, changes in the meteorology seem to indicate two active processes ongoing that appear to support the

435   formation of low clouds after a clear sky period; namely horizontal advection (dynamic forcing) and quiescent air mass modification (local forcing). Variable dynamics resulting in differential atmospheric advection is most prominently observed during the winter and early spring. During these seasons, near-surface wind directions had the largest variability from the time of cloud dissipation to the time of subsequent cloud formation. Such shifts in wind are indicative of transient disturbances impacting the NSA. A case study of low-level mid-spring cloud lifecycle from Barrow also found the

440   dissipation of the cloud layer was associated with converging air masses from different origins (Kalesse et al., 2016). Trends in near-surface temperature during the latter part of the clear sky periods reveal a near universal drop in temperatures, which may be associated with strong infrared cooling to space under clear skies; the cooling trends may also be supported by cold air advection in connection with synoptic forcing. Corresponding trends in dew point depressions during winter and spring were primarily absent, indicating that as the temperature dropped, so did the moisture content, likely due to the synoptic

445   advection of drier air locally around Barrow. Despite the active synoptic forcing signals during winter and spring, changes in near-surface aerosol number concentrations were generally absent; particle number concentrations were relatively constant just before and just after cloud dissipation (Figs. 6a-b and 7e-f).

During summer, near-surface aerosol number concentrations and meteorological trends during the clear periods had different

450   characteristics compared to winter and spring. Generally, particle numbers were larger immediately after cloud dissipation (compared to immediately before) and this trend continued through the clear period such that number concentrations were also larger immediately before clouds formed (in comparison to after they formed). The lower tropospheric stability of the lower atmosphere was not as strongly stratified in summer as it was during winter/spring, but higher concentrations of near-surface particles were observed with increased stratification during summer and early autumn, a signal that was not observed

455   during winter and spring. The increased stability may suppress vertical mixing and hence the aerosols may be constrained to the shallow surface layer. Furthermore, trends in near-surface dew point depression followed the trends in near-surface temperature in the hours preceding cloud formation. These consistent thermodynamic changes indicate the lower atmosphere is approaching saturation as a result of air mass cooling, not necessarily due to increased moisture content through horizontal advection.

460

While large scale geopotential height tendencies showed active differential advection occurring in summer and early autumn, prior to cloud formation the clear period geopotential tendencies over the lower 700-850 hPa atmospheric layer were smaller in magnitude than for the other seasons. Wind directions also remained mostly stationary for the duration of the clear periods during summer, further indicating that large-scale synoptic shifts were uncommon and likely not the determining factor for

465 cloud formation events. Taken altogether, these lower atmospheric phenomena represent quiescent air mass modification processes, by which the relative paucity of large-scale forcing permits the surface layer to cool and approach saturation all the while aerosol particle concentrations remained sufficiently large and constrained across the lower atmosphere.

Low cloud or fog formation events marking the end of the clear periods were the most frequent during late spring, summer

470 and autumn; in winter low clouds or fog after clear periods did occur but were the minority. The enhancement of aerosol particle concentrations near the surface, together with near-surface cooling and relative humidity increases, are consistent with ongoing air mass modification processes that actively support the formation of low clouds, especially during summer. The formation of low clouds or fog bookending an Arctic clear sky period may bear similarity to the relatively nonturbulent, optically thin clouds reported in Sedlar (2014) and Silber et al. (2020). During the cold, darker seasons, the low cloud or fog

475 formations may in fact be ice fogs, a common occurrence in the Arctic (e.g., Gultepe et al., 2014; 2017).

The air mass modification process has been described by Tjernström et al. (2019) for warm, moist air mass that is transported from continental/open ocean in over Arctic sea ice; such a process, where low clouds form at or very near the surface and gradually rise and develop turbulent circulations through radiative divergence has been proposed by Herman and

480 Goody (1976). Here, a similar transformation process has been identified on the northern edge of NSA. The modification of the air mass is not dependent upon sea ice at the surface to drive the air mass transformation, but instead radiative cooling from the terrestrial surface under modestly active or quiescent atmospheric conditions supports the cooling and moisture loading. To our knowledge, this study is a first in examining the how atmospheric processes and aerosol partitioning during clear periods influence the formation of clouds that mark the cessation of a clear period. Considering the high frequency and

485 long persistence of low clouds measured at Arctic observatories (Shupe et al., 2011), we hypothesize that the formation of the clouds, especially during the late spring through early autumn, initially began as surface-based, or near surface-based low clouds and fog (Silber et al., 2020). As the cloud lifecycle matures, vertical turbulent mixing of and horizontal advection lift the cloud layer, resulting in the morphology into the prototypical Arctic mixed-phase stratocumulus cloud.

6 Conclusions

A suite of in situ and remote sensing measurements and data products from the NSA have been analysed to determine the processes contributing to low cloud dissipation and formation events. The triggering mechanisms that support the cloud dissipation and formation events are important because they effectively commence or end a clear sky period. These clear sky periods have a profound impact on the surface energy budget, which further impacts the stratification of the lower troposphere. Improved understanding on Arctic clear period evolution has impacts on scales relevant to local weather and climate.

We conclude that the onset of clear sky periods, and subsequently the end of clear periods, are primarily responsive to transient atmospheric forcing. While we report that all months are subjected to synoptic disturbances, the magnitude of the forcing is weaker during late spring and through early autumn than during winter and early spring. Relatively homogeneous near-surface thermodynamics and winds during clear sky periods lends support to predominant quiescent conditions during the summer months. The weaker forcing promotes the near-surface temperature to drop through infrared radiative cooling to space, causing the temperature to more rapidly approach the dew point temperature, ultimately increasing relative humidity.

At the same time, increased pooling of aerosol particles near the surface provides the ingredients for the environment to support condensation (potentially ice fog during cold months). Air mass changes are likely not the cause for increasing near-surface aerosol concentrations since the thermodynamics and winds during the summer time clear-sky periods revealed little variability. Instead, enhanced stable stratification resulting from a lack of low cloud cover supports the pooling of aerosols in a shallower boundary layer closer to the surface.

The mechanisms leading to cloud dissipation are less transparent. Statistics of aerosol backscatter from the HSRL shortly after cloud dissipation indicated aerosol backscatter was smaller in the layer where the cloud was previously observed, compared to below the cloud layer. While this may indicate a reduction in aerosol from near, or above cloud top, as critical in causing its dissipation, it is impossible to analyse the backscatter evolution prior to cloud dissipation because the HSRL signal is attenuated by the cloud layer. At the same time, we did find relatively active geopotential height tendencies in the radiosoundings prior to cloud dissipation. A frontal passage or air mass trajectory change, like that reported to have caused the dissipation in Kalesse et al. (2016), cannot be ruled out. Currently, we are examining the potential validity of aerosol changes in causing Arctic cloud dissipation with the help of cloud resolving model simulations that incorporate detailed aerosol physics. Detailed case studies will be explored to address the impacts of varying aerosol number, vertical

520 partitioning, and hygroscopic properties on cloud dissipation, and furthermore on the formation of low-level clouds or fog, which have been shown in this study to be the dominant Arctic cloud type following clear sky periods.

Acknowledgements

525 This research has been supported by the U.S. Department of Energy's (DoE) Office of Biological and Environmental Research (BER) Atmospheric Systems Research grant no. DE-SC0019073.

Data Availability

530 All observations analysed in this study are freely available to the user community by following the links provided here to their respective repositories. The ceilometer measurements are accessible from the ARM Data Archive: https://adc.arm.gov/discovery/#/results/s::nsaceilC1.b1. The HSRL observations are accessible from the ARM Data Archive: https://adc.arm.gov/discovery/#/results/s::nsahsrlC1.a1. The cloud boundaries derived from the ARSCL processing algorithms from the KAZR are accessible from the ARM Data Archive:

535 https://adc.arm.gov/discovery/#/results/s::nsaarsclkazr1kolliasC1. The. RadFlux surface radiation measurements and data products are accessible from the ARM Data Archive: https://adc.arm.gov/discovery/#/results/datastream::nsaradflux1longC1.c1. The radiosoundings are accessible from the ARM Data Archive: https://adc.arm.gov/discovery/#/results/s::nsasondewnpnC1.b1. Near-surface meteorology measurements are accessible from the ARM Data Archive: https://adc.arm.gov/discovery/#/results/s::nsametC1.b1. Finally, near-surface CPC

540 measurements are accessible from the NOAA Global Monitoring Laboratory ftp server: https://www.esrl.noaa.gov/gmd/dv/data/index.php?parameter_name=Aerosols&site=BRW.

References

545 Avramov, A. and Harrington, J.Y., Influence of parameterized ice habit on simulated mixed phase Arctic clouds, *J. Geophys. Res.*, **115**, D03205, doi:10.1029/2009JD012108, 2010.

Birch, C.E. and coauthors, Modelling atmospheric structure, cloud and their response to CCN in the central Arctic: ASCOS case studies, *Atmos. Chem. Phys.*, **12**, 3419-3435, doi:10.5194/acp-12-3419-2012, 2012.

550

Brooks, I.M., Tjernström, M., Persson, P.O.G., Shupe, M.D., Atkinson, R.A., Canut, G., Birch, C.E., Mauritsen, T., Sedlar, J. and Brooks, B.J., The Turbulent Structure of the Arctic Summer Boundary Layer During the Arctic Summer Cloud-Ocean Study, *J. Geophys. Res. Atmos.*, **122**, 9685-9704, doi:10.1002/2017JD027234, 2017.

555 Curry, J.A., Rossow, W.B., Randall, D. and Schramm, J.L., Overview of Arctic Cloud and Radiation Characteristics, *J. Clim.*, **9**, 1731-1764, 1996.

Di Pierro, M., Jaeglè, L., Eloranta, E.W. and Sharma, S., Spatial and seasonal distribution of Arctic aerosols observed by the CALIOP satellite instrument (2006-2012), *Atmos. Chem. Phys.*, **13**, 7075-7095, doi:10.5194/acp-13-7075-2013, 2013.

560

Eloranta, E.W., "High Spectral Resolution Lidar", in Lidar: Range-Resolved Optical Remote Sensing of the Atmosphere, K. Weitkamp editor, Springer-Verlag, New York, 2005.

Engström, A., Karlsson, J. and Svensson, G., The Importance of Representing Mixed-Phase Clouds for Simulating

565 Distinctive Atmospheric States in the Arctic, *J. Clim.*, **27**, 265-272, doi:10.1175/JCLI-D-13-0027.1, 2014.

Gultepe, I., Kuhn, T., Pavolonis, M., Calvert, C., Gurka, J., Heymsfield, A.J., Liu, P.S.K., Zhou, B., Ware, R., Ferrier, B., Milbrandt, J. and Bernstein, B., Ice Fog in Arctic During FRAM-Ice Fog Project: Aviation and Nowcasting Applications, *Bull. Amer. Meteorol. Soc.*, **95**, 211-226, doi:10.1175/BAMS-D-11-00071.1, 2014.

570

Gultepe, I., Heymsfield, A.J., Gallagher, M., Ickes, L. and Baumgardner, D., Ice Fog: The Current State of Knowledge and Future Challenges, *Meteorol. Mongr.*, **58**, 4.1-4.24, doi:10.1175/AMSMONOGRAPHS-D-17-0002.1, 2017.

Harrington, J.Y., Reisin, T., Cotton, W.R. and Kreidenweis, S.M., Cloud resolving simulations of Arctic stratus. Part II:

575 Transition-season clouds, *Atmos. Res.*, **51**, 45-75, 1999.

Herman, G. and Goody, R., Formation and Persistence of Summertime Arctic Stratus Clouds, *J. Atmos. Sci.*, **33**, 1537-1553, 1976.

580 Holton, J.R., *An Introduction to Dynamic Meteorology*, Third Edition, Renata Dmowska editor, Academic Press, 1992.

Igel, A.L., Ekman, A.M.L., Leck, C., Tjernström, M., Savre, J. and Sedlar, J., The free troposphere as a potential source of arctic boundary layer aerosol particles, *Geophys. Res. Lett.*, **44**, 7053-7060, doi:10.1002/2017GL073808, 2017.

585 Intrieri, J.M., Shupe, M.D., Uttal, T. and McCarty, B.J., An annual cycle of Arctic cloud characteristics observed by radar and lidar at SHEBA, *J. Geophys. Res.*, **107**, No. C10, doi:10.1029/2000JC000423, 2002.

Jiang, H., Cotton W.R., Pinto, J.O., Curry, J.A. and Weissbluth, M.J., Cloud resolving simulations of mixed-phase Arctic stratus observed during BASE: Sensitivity to concentration of ice crystals and large-scale heat and moisture advection, *J. Atmos. Sci.*, **57**, 2105-2117, 2000.

590

Kafle, D.N. and Coulter, R.L., Micropulse lidar-derived aerosol optical depth climatology at ARM sites worldwide, *J. Geophys. Res.*, **118**, 7293-7308, doi:10.1002/jgrd.50536, 2013.

595   Kahl, J.D., Characteristics of the Low-Level Temperature Inversion Along the Alaskan Arctic Coast, *Int. J. Climatol.*, **10**, 537-548, 1990.

Kalesse, H., de Boer, G., Solomon, A., Que, M., Ahlgrimm, M., Zhang, D., Shupe, M.D., Luke, E. and Protat, A., Understanding Rapid Changes in Phase Partitioning between Cloud Liquid and Ice in Stratiform Mixed-Phase Clouds:

600   An Arctic Case Study, *Mon. Wea. Rev.*, **144**, 4805-4826, doi:10.1175/MWR-D-16-0155.1, 2016.

Kay, J.E., L'Ecuyer, T., Chepfer, H., Loeb, N, Morrison, A. and Cesana, G., Recent Advances in Arctic Cloud and Climate Research, *Curr. Clim., Change Rep.*, **2**, 159-169, doi:10.1007/s40641-016-0051-9, 2016.

605   Klonecki, A., Hess, P. Emmons, L.K., Smith, L., Orlando, J.J. and Blake, D., Seasonal changes in the transport of pollutants into the Arctic troposphere-model study, *J. Geophys Res. Atmos.*, **108**, D4, doi:10.1029/2002JD002199, 2003.

Kollias, P. and coauthors, Chapter 17. Development and Applications of ARM Millimeter-Wavelength Cloud Radars, Meteorol. Monographs, **57**, 17.1-17.19, doi:10.1175/AMSMONOGRAPHS-D-15-0037.1, 2016.

610

Loewe, K., Ekman, A.M.L., Paukert, M., Sedlar, J., Tjernström, M. and Hoose, C., Modelling micro- and macrophysical contributors to the dissipation of an Arctic mixed-phase cloud during the Arctic Summer Cloud Ocean Study (ASCOS), *Atmos. Chem. Phys.*, **17**, 6693-6704, doi:10.5194/acp-17-6693-2017, 2017.

615

Long, C.N. and Turner, D.D., A method for continuous estimation of clear-sky downwelling longwave radiative flux developed using ARM surface measurements, *J. Geophys. Res.*, **113**, D18206, doi:10.1029/2008JD009936, 2008.

Moran, K.P., Martner, B.E., Post, M.J., Kropfli, R.A., Welsh, D.C. and Widener, K.B., An Unattended Cloud-Profiling

620   Radar for Use in Climate Research, *Bull. Amer. Meteorol. Soc.*, **79**, No. 3, 443-455, 1998.

Morrison, H. and coauthors, Intercomparison fo cloud model simulations of Arctic mixed-phase boundary layer clouds observed during SHEBA/FIRE-ACE, *J. Adv., Model., Earth Syst.*, **3**, doi:10.1029/2011MS000066, 2011.

625 Morrison, H., de Boer, G., Feingold, G., Harrington, J., Shupe, M.D. and Sulia, K., Resilience of persistent Arctic mixed-phase clouds, *Nature Geosci.*, **5**, 11-17, doi:10.1038/NGEO1332, 2012.

Pinto, J.O., Curry, J.A. and Fairall, C.W., Radiative characteristics of the Arctic atmosphere during spring as inferred from ground-based measurements, *J. Geophys. Res.*, **102**, No. D6, 6941-6952, 1997.

630

Pithan, F., Medeiros, B. and Mauritsen, T., Mixed-phase clouds cause climate model biases in Arctic wintertime temperature inversions, *Clim., Dyn.*, **43**, 289-303, doi:10.1007/s00382-013-1964-9, 2014.

Ravila, P. and Räsänen, J., New laser ceilometer using enhanced single lens optics, Eighth Symposium on Integrated
635 Observing and Assimilation Systems for Atmosphere, Oceans, and Land Surface at 84th AMS Annual Meeting (Seattle, WA), https://ams.confex.com/ams/84Annual/techprogram/paper_68092.htm, 2004.

Sedlar, J., Tjernström, M., Mauritsen, T., Shupe, M.D., Brooks, I.M., Persson, P.O.G., Birch, C.E., Leck, C., Sirevaag, A. and Nicolous, M., A transitioning Arctic surface energy budget: the impacs of solar zenith angle, surface albedo and
640 cloud radiative forcing, *Clim. Dyn.*, **37**, 1643-1660, doi:10.1007/s00382-010-0937-5, 2011.

Sedlar, J. and Devasthale, A., Clear-sky thermodynamic and radiative anomalies over a sea ice sensitive region of the Arctic, *J. Geophys. Res.*, **117**, D19111, doi:10.1029/2012JD017754, 2012.

645 Sedlar, J., Implications of Limited Liquid Water Path on Static Mixing within Arctic Low-Level Clouds, *J. Appl. Meteorol. Climatol.*, **53**, 2775-2789, doi:10.1175/JAMC-D-14-0065.1, 2014.

Sedlar, J. and Shupe, M.D., Characteristic nature of vertical motions observed in Arctic mixed-phase stratocumulus, *Atmos. Chem. Phys.*, **14**, 3461-3478, doi:10.5194/acp-14-3461-2014, 2014.

650

Sedlar, J. and coauthors, Confronting Arctic Troposphere, Clouds, and Surface Energy Budget Representations in Regional Climate Models With Observations, *J. Geophys. Res. Atmos.*, **124**, doi:10.1029/2019JD031783, 2020.

Shupe, M.D. and Intrieri, J.M., Cloud Radiative Forcing of the Arctic Surface: The Influence of Cloud Properties, Surface
655 Albedo, and Solar Zenith Angle, *J. Clim.*, **17**, 616-628, 2004.

Shupe, M.D., Kollias, P., Matrosov, S.Y. and Schneider, T.L., Deriving Mixed-Phase Cloud Properties from Doppler Radar Spectra, *J. Atmos. Oceanic Technol.*, **21**, 660-670, 2004.

660   Shupe, M.D., A ground-based multisensory cloud phase classifier, *Geophys. Res. Lett.*, **34**, L22809, doi:10.1029/2007GL031008, 2007.

Shupe, M.D., Kollias, P., Persson, P.O.G. and McFarquhar, G.M., Vertical Motions in Arctic Mixed-Phase Stratiform Clouds, *J. Atmos. Sci.*, **65**, 1304-1322, doi:10.1175/2007JAS2479.1, 2008.

665

Shupe, M.D., Clouds at Arctic Atmospheric Observatories. Part II: Thermodynamic Phase Characteristics, *J. Appl. Meteorol. Climatol.*, **50**, 645-661, doi:10.1175/2010JAMC2468.1, 2011.

Shupe, M.D., Walden, V.P., Eloranta, E., Uttal, T., Campbell, J.R., Starkweather, S.M. and Shiobara, M., Clouds at Arctic
670   Atmospheric Observatories. Part I: Occurrence and Macrophysical Properties, *J. Appl. Meteorol., Climatol.*, **50**, 626-644, doi:10.1175/2010JAMC2467.1, 2011.

Shupe, M.D., Persson, P.O.G., Brooks, I.M., Tjernström, M., Sedlar, J., Mauritsen, T., Sjogren, S. and Leck, C., Cloud and boundary layer interactions over the Arctic sea ice in late summer, *Atmos. Chem. Phys.*, **13**, 9379-9400,
675   doi:10.5194/acp-13-9379-2013, 2013.

Silber, I., Fridlind, A.M., Verlinde, J., Russell, L.M. and Ackerman, A.S., Nonturbulent Liquid-Bearing Polar Clouds: Observed Frequency of Occurrence and Simulated Sensitivity to Gravity Waves, *Geophys. Res. Lett.*, **47**, doi:10.1029/2020GL087099, 2020.

680

Sotiropoulou, G., Sedlar, J., Tjernström, M., Shupe, M.D., Brooks, I.M. and Persson, P.O.G., The thermodynamic structure of summer Arctic stratocumulus and the dynamic coupling to the surface, *Atmos. Chem. Phys.*, **14**, 12573-12595, doi:10.5194/acp-14-12573-2014, 2014.

685   Stevens, R.G. and coauthors, A model intercomparisons of CCN-limited tenuous clouds in the high Arctic, *Atmos. Chem. Phys.*, **18**, 11041-11071, doi:10.5194/acp-18-11041-2018, 2018.

Stramler, K., Del Genio, A.D. and Rossow, W.B., Synoptically Driven Arctic Winter States, *J. Clim*, **24**, 1747-1762, doi:10.1175/2010JCLI3817.1, 2011.

690

Tjernström, M., Shupe, M.D., Brooks, I.M., Achtert, P., Prytherch, J. and Sedlar, J., Arctic Summer Airmass Transformation, Surface Inversions, and the Surface Energy Budget, *J. Clim.*, **32**, 769-789, doi:10.1175/JCLI-D-18-0216.1, 2019.

695 Walsh, J.E. and Chapman, W.L., Arctic Cloud-Radiation-Temperature Associations in Observational Data and Atmospheric Reanalysis, *J. Clim.*, **11**, 3030-3045, 1998.

Wang, X. and Key, J.R., Arctic Surface, Cloud, and Radiation Properties Based on the AVHRR Polar Pathfinder Dataset. Part I: Spatial and Temporal Characteristics, *J. Clim.*, **18**, 2558-2574, 2005.

700

Willis, M., Leaitch, R. and Abbatt, J., Atmospheric aerosol in the changing Arctic, *Eos*, **99**, doi:10.1029/2018EO108619, 2018.

705
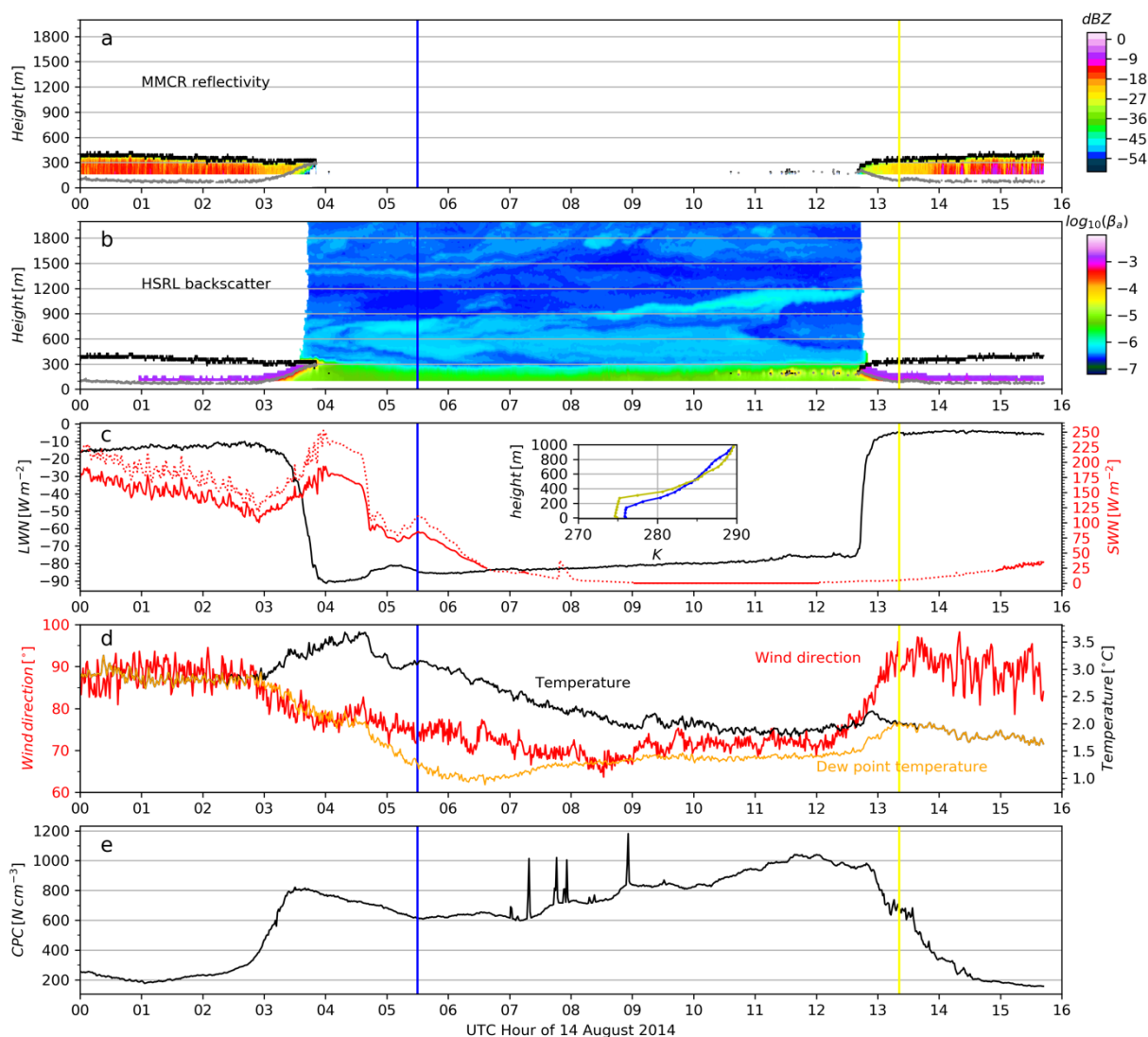
Figure 1: Temporal evolution of cloud dissipation, a clear sky period, and the formation of a cloudy period from 14 August 2014 from the North Slope of Alaska. a) KAZR reflectivity [dBZ, contours] and cloud top (black) and base height (gray) boundaries. b) HSRL backscatter [log10(Ba)] including cloud top and base boundaries; c) Net longwave (black) and net shortwave (red) radiation, including downwelling shortwave (dashed red), all in W m⁻²; the inset includes equivalent potential temperature [K] profiles from radiosoundings at 05:30 (blue) and 13:15 UTC (yellow); the vertical blue and yellow lines in each panel represent the radiosounding launch time. d) Near surface wind direction [degrees, red], temperature [K, black] and dew point temperature [K, orange]. e) Near surface particle concentration [N/cm³].
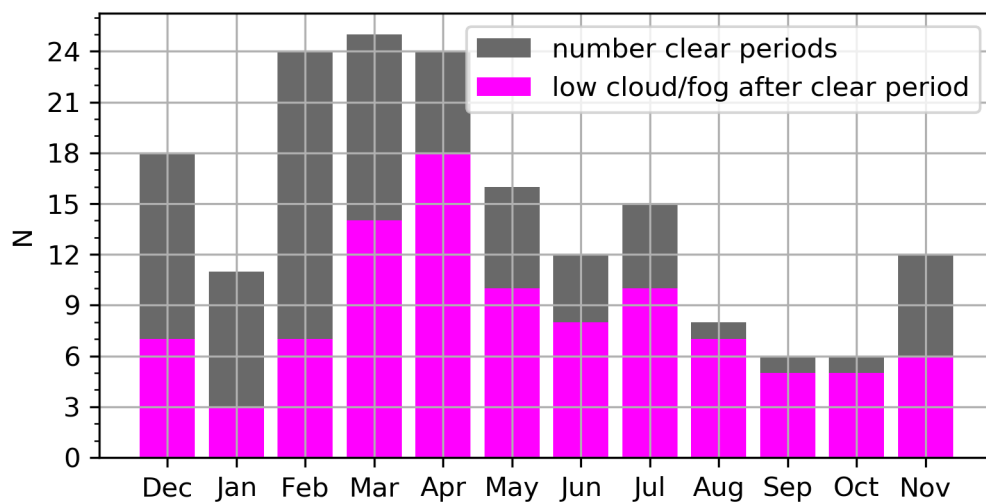
715

Figure 2: Monthly occurrences of strict clear sky periods determined from the remote sensing suite at ARM-NSA during 2014 to 2018 (gray bars). Magenta bars represent the number of clear sky periods that ended with the emergence of a surface-based fog or low cloud layer with a cloud base below 400 m AGL.
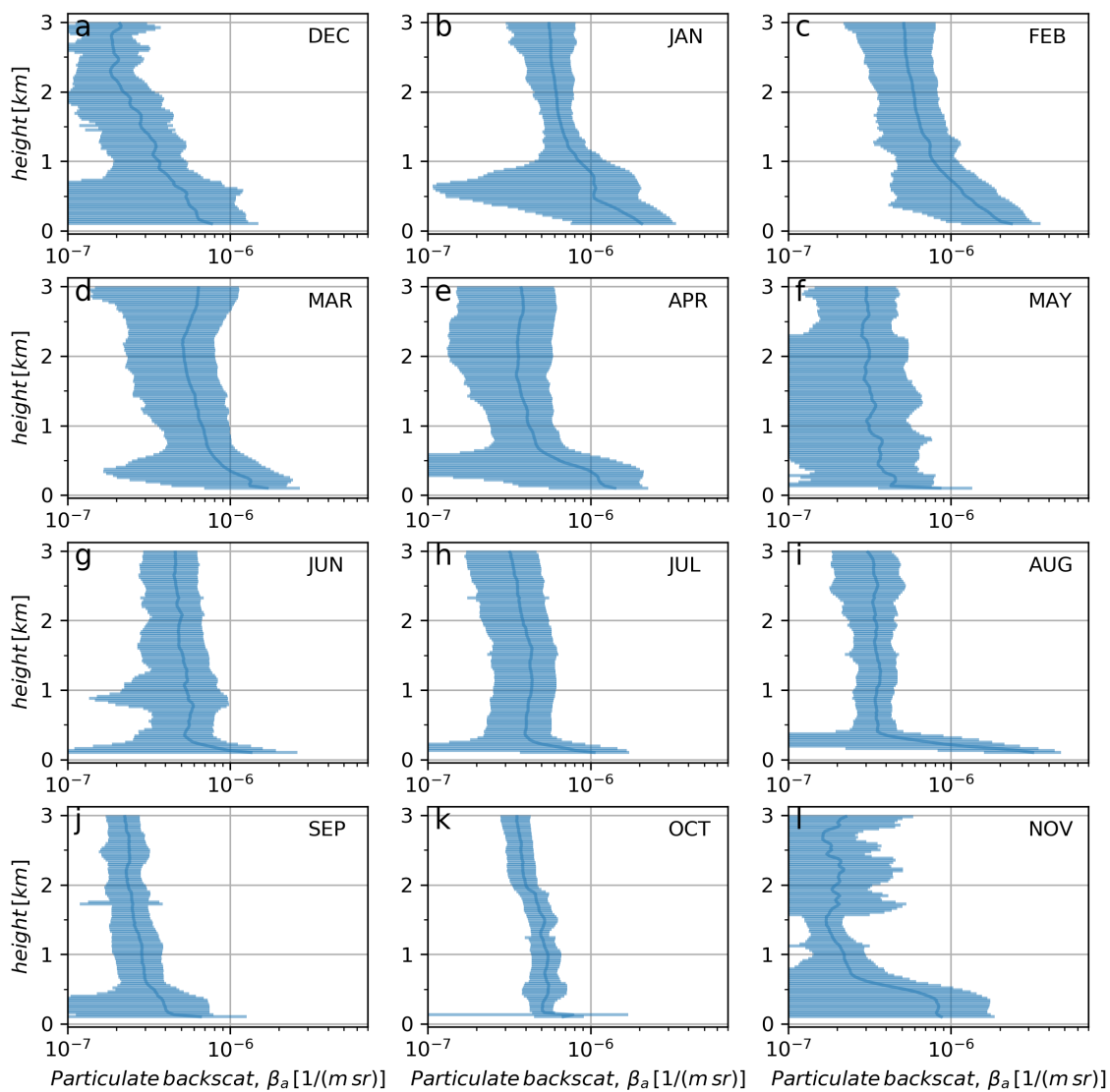
720

Figure 3: Monthly mean and 1-sigma HSRL backscatter [1/(m sr)] profiles up to 3 km AGL during clear sky periods. Rows are arranged seasonal from top to bottom: a-c) DJF, d-f) MAM, g-i) JJA, and j-l) SON.
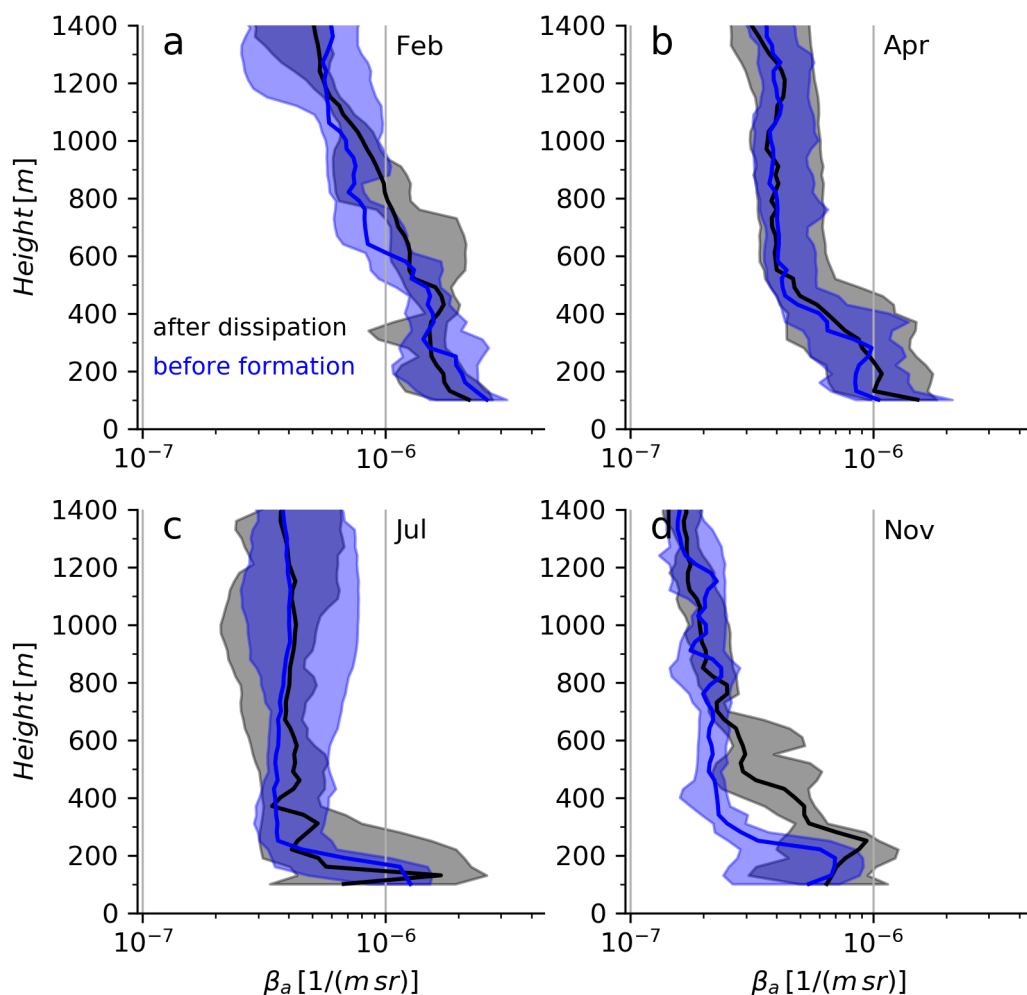
Figure 4: Median (solid line) and interquartile range (shading) profiles of clear-sky aerosol backscatter [1/(m sr)] only for clear periods when a low cloud (base < 400 m) or surface fog was observed to form. Black (gray shading) profiles are for backscatter within 30-60 min period after cloud dissipation; blue (light blue shading) profiles are for backscatter within 60 to 30 min prior to low cloud formation.
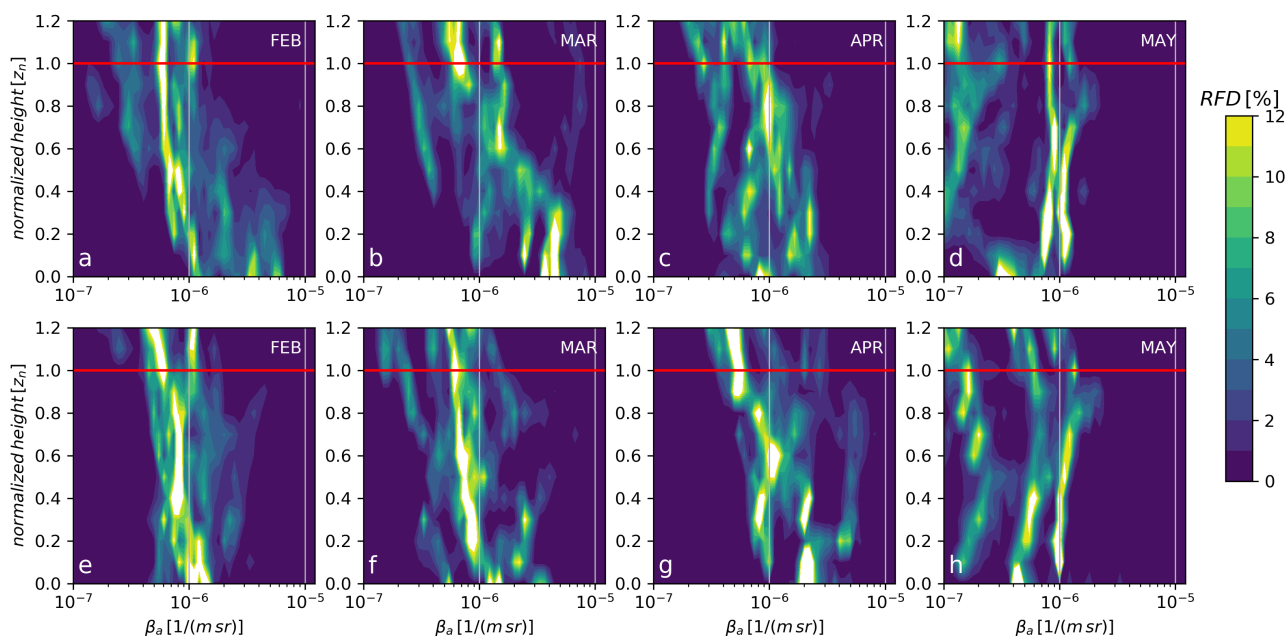
730

Figure 5: RFDs [%, colors] of aerosol backscatter as a function of normalized height, z_n, where $z_n = 0$ is the surface and $z_n = 1$ is the former/successive mean cloud top height surrounding the clear sky period. All HSRL backscatter profiles after/before 60 minutes of cloud dissipation/formation are combined to create the frequency distributions, which are normalized to 100% at each normalized height range. Distributions for February, March, April and May are shown for a-d) after cloud dissipation (start of clear period), and e-h) prior to cloud formation (end of clear period).
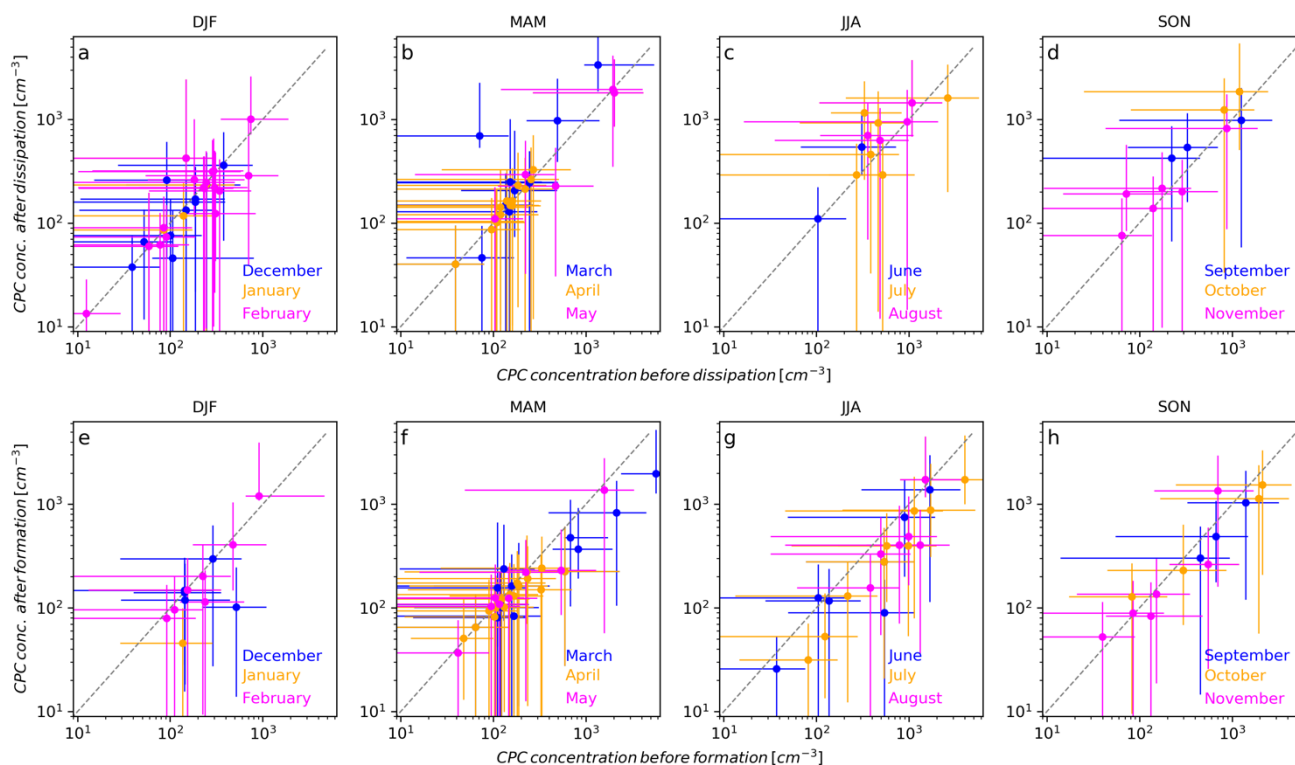
Figure 6: Median (circles) and interquartile range (lines) of CPC concentrations [cm⁻³] in 2 hr period after cloud dissipation versus 2 hr period before cloud dissipation (a-d), and 2 hr period after cloud formation versus 2 hr period before cloud formation (e-f).
740 **Monthly cases are in colors and labeled in each subpanel, with the months group by season from left to right: DJF, MAM, JJA, and SON. The 1:1 gray dashed line is included as a reference. Note the logarithmic axes.**
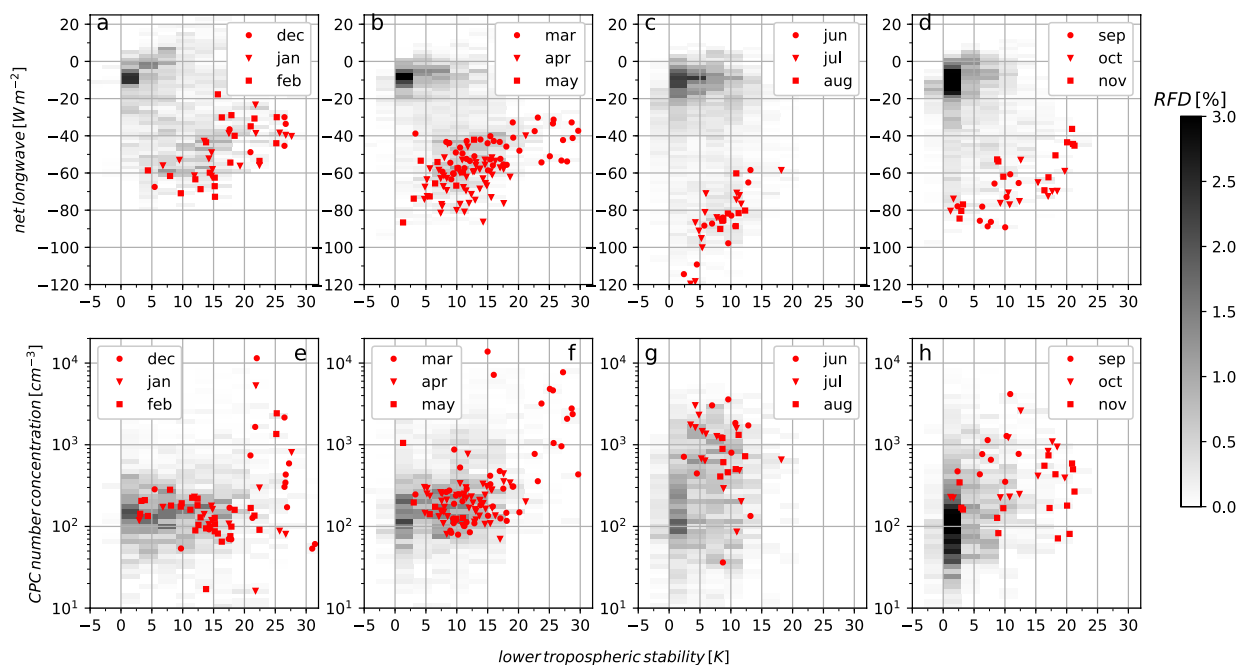
Figure 7: Relative frequency distributions (RFDs, gray contours) of a-d) net longwave radiation (LWN, [W m⁻²]) as a function of lower tropospheric stability (LTS, [K]) for a) winter, b) spring, c) summer, and d) autumn. e-f) Relative frequency distributions of near-surface CPC concentrations [cm⁻³] as a function of LTS. LWN and CPC concentrations are taken within 10 min of each radiosounding profile used to estimate LTS. Red symbols represent the individual relationships between LTS and LWN/CPC values within 10 min of the radiosounding during the clear sky periods; each month within the season is represented by a different symbol.
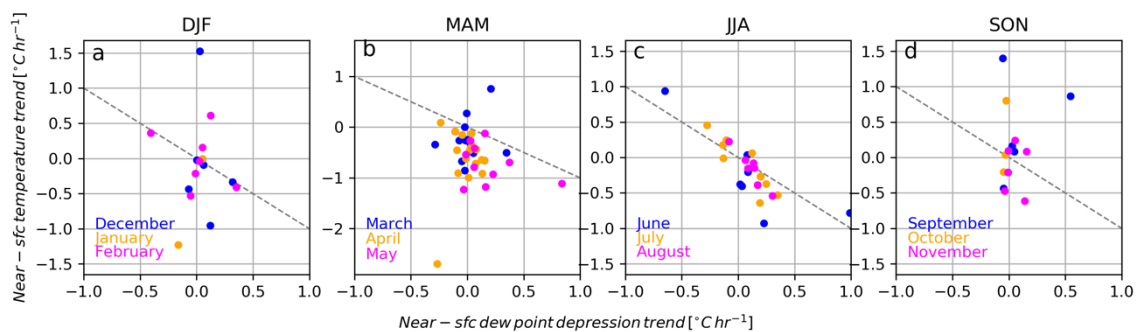
Figure 8: Linear trends in near surface air temperature [°C hr⁻¹] versus linear trend in dew point depression [°C hr⁻¹] computed using linear regression of temperatures in a 4-hr period prior to low cloud/fog formation. Dew point depressions are computed as the dew point temperature minus the air temperature. A positive dew point depression trend indicates a deceasing difference in dew point and air temperatures.
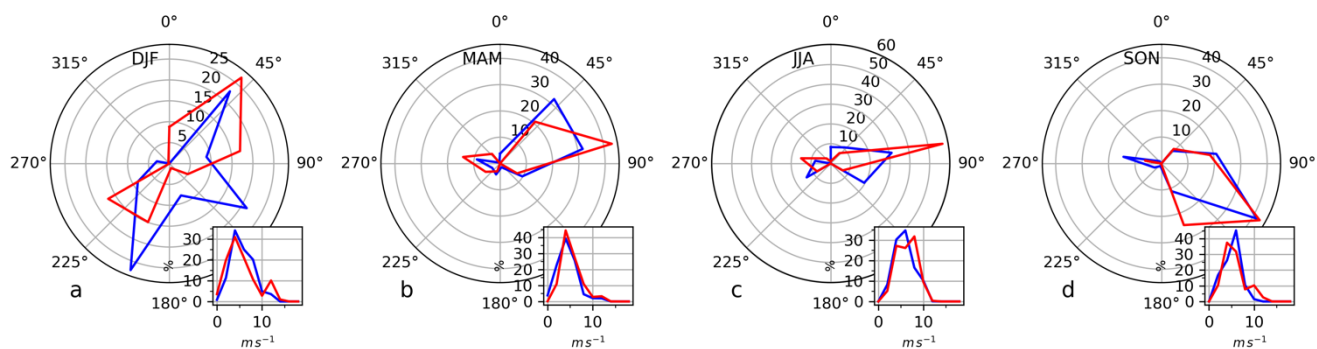
Figure 9: Seasonal RFDs (radii, [%]) of near-surface wind direction [degrees] within 1-hr after cloud dissipation (red) and within 1-hr of low cloud/fog formation (blue) for a) DJF, b) MAM, c) JJA, and d) SON. Inserts in each panel show the RFD of wind speed [m s^{-1}].
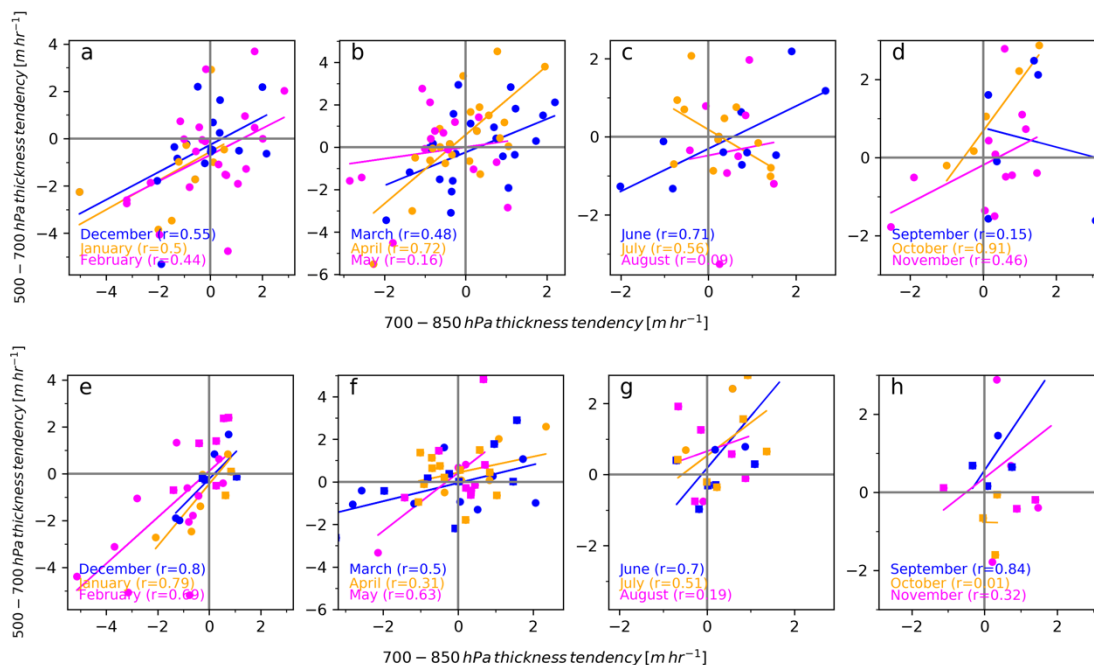
Figure 10: Geopotential height thickness tendencies [m hr⁻¹] of two atmospheric layers, 500-700 hPa and 700-850 hPa leading up to cloud dissipation (a-d) and cloud formation (e-f). Tendencies are computed from layer thicknesses from the two radiosounding

765 **profiles immediately prior to cloud dissipation (but not before dissipation) and immediately before cloud formation (but not after formation). In e-f) the squares indicate the layer thickness tendency relationship when a low cloud/fog was observed as the forming cloud. Colored lines are the least squares linear fit to the data for each month, with correlations (r-values) listed in each panel.**